INTERNAL AND EXTERNAL AXIAL CORNER FLOWS

By Paul Kutler,
NASA Ames Research Center

Vijaya Shankar, Dale A. Anderson,
Iowa State University

and Reese L. Sorenson
NASA Ames Research Center

SUMMARY

The inviscid, internal and external axial corner flows generated by two intersecting wedges traveling supersonically are obtained by use of a second-order shock-capturing, finite-difference approach. The governing equations are solved iteratively in conical coordinates to yield the complicated wave structure of the internal corner and the simple peripheral shock of the external corner. The numerical results for the internal flows compare favorably with existing experimental data.

INTRODUCTION

Existing supersonic aircraft such as the B-1, F-14, F-15, Concorde, and recently proposed designs of advanced hypersonic research aircraft such as that shown in figure 1, possess engine inlets which are composed of planar compression or expansion surfaces with swept and unswept leading edges. These surfaces form various combinations of internal and external axial corners. Such a corner configuration can generate a rather complicated interference flowfield whose prediction is of considerable interest to the vehicle designer, because of the severe pressure gradients and high local heating that can occur at the surface.

The typical internal corner configuration studied in this paper and the coordinate system used are shown in figure 2. The flow direction is aligned with the x-axis. The vertical wedge is unswept and is always considered a compression surface; i.e., $\delta_2 > 0$. The horizontal or base wedge can have a sweep of Λ and be either a compression or an expansion surface; i.e., $\delta_1 \lessgtr 0$.

The conical wave structure for a typical swept, compression-compression configuration is also shown in figure 2. The shock structure consists of a planar shock emanating from the leading edge of each wedge, a corner shock that joins the two wedge shocks, and two embedded shocks that stretch from the body to the triple points. A slip surface exists between each of the triple points and the axial corner at which there exists a vortical singularity.

If the base wedge is an expansion surface; i.e., $\delta_1 > 0$, then a Prandtl-Meyer expansion fan emanates from the leading edge and intersects the vertical wedge shock perpendicularly. As a result of the interaction, the wedge shock is bent and shifted slightly towards the axial corner, becoming weakened in the process. The expansion fan, after interaction with the wedge shock, becomes concave with respect to the corner.

A typical external corner configuration is shown in figure 3 and consists of two intersecting compression surfaces with angles δ_1 and δ_2 and sweeps Λ_1 and Λ_2. The flow structure about the external corner is considerably simpler than that of the internal corner. It consists of a single continuous shock wave whose strength in rounding the corner transitions from that of the δ_1-wedge shock to that of the δ_2-wedge shock. Like the internal-flow problem, there also exists a vortical singularity at the axial corner due to the convergence of the cross-flow streamlines (each with different values of entropy).

Both the internal and external axial corner flows are conical since there is no characteristic length associated with the body. Viscous effects are assumed to be minimal, and therefore the flow is governed by the three-dimensional steady-flow Euler equations. These equations, under a nonorthogonal coordinate transformation which introduces conical self-similarity and aligns certain independent variables with the body, are hyperbolic and can be integrated in an iterative fashion using MacCormack's finite-difference algorithm (ref. 1). The internal corner problem with its complicated wave structure is solved using the shock-capturing philosophy (ref. 2) while the external corner problem with its single peripheral shock is solved using both the shock-capturing and shock-fitting approaches.

THEORY

The governing partial differential equations (continuity, x, y, and z momentum) in Cartesian coordinates (see figs. 2 and 3) are first written in the dimensionless strong conservation-law form:

$$E_x^{**} + F_y^{**} + G_z^{**} = 0 \tag{1}$$

where

$$E^{**} = \begin{bmatrix} \rho u \\ kp + \rho u^2 \\ \rho uv \\ \rho uw \end{bmatrix} \qquad F^{**} = \begin{bmatrix} \rho v \\ \rho uv \\ kp + \rho v^2 \\ \rho vw \end{bmatrix} \qquad G^{**} = \begin{bmatrix} \rho w \\ \rho uw \\ \rho vw \\ kp + \rho w^2 \end{bmatrix}$$

and where $k = (\gamma-1)/2\gamma$, γ being the ratio of specific heats.

In equation (1), pressure p and density ρ are made dimensionless with respect to free-stream stagnation conditions, and velocity components u, v, and w are made dimensionless with respect to the maximum adiabatic velocity. The above system of equations is made complete by the addition of the steady-flow energy equation which can be written in the following dimensionless form:

$$p = \rho\left(1 - u^2 - v^2 - w^2\right) \tag{2}$$

It is desirable when solving fluid flow problems to transform the independent variables so that the new coordinates are aligned with the surface of the body. This alleviates the numerical difficulties associated with satisfying the tangency conditions for an unequally spaced grid. A transformation which satisfies the above criterion and also includes conical self-similarity is

$$\left.\begin{aligned} \zeta &= x \\ \eta &= y/(x - z \tan \Lambda_1) \\ \xi &= z/(x + y \tan \Lambda_2) \end{aligned}\right\} \tag{3}$$

where Λ_1 and Λ_2 are depicted in figure 3 for the external corner. For the internal corner, $\Lambda_1 = \Lambda$ and $\Lambda_2 = 0$.

Under the above transformation equation (1) becomes

$$E_\zeta^* + F_\eta^* + G_\xi^* + H^* = 0 \tag{4}$$

where

$$E^* = E^{**}cd$$

$$F^* = -E^{**}\eta c + F^{**}c + G^{**}\eta c + \tan \Lambda_1$$

$$G^* = -E^{**}\xi d - F^{**}\xi d \tan \Lambda_2 + G^{**}d$$

$$H^* = E^*[-c(-b +(\xi/e))\tan \Lambda_1 - d(a -(\eta/e))\tan \Lambda_2]$$
$$\quad + F^*[-d(-1 +(1/e))\tan \Lambda_2 - \xi(c/e)\tan \Lambda_1 \tan \Lambda_2]$$
$$\quad + G^*[-c(1 -(1/e))\tan \Lambda_1 - \eta(d/e)\tan \Lambda_1 \tan \Lambda_2]$$

$$a = \eta(1 - \xi \tan \Lambda_1)/e$$

$$b = \xi(1 + \eta \tan \Lambda_2)/e$$

$$c = \zeta(1 + a \tan \Lambda_2)$$

$$d = \zeta(1 - b \tan \Lambda_1)$$

$$e = 1 + \eta\xi \tan \Lambda_1 \tan \Lambda_2$$

Thus equation (4) governs the flow over both the internal and external corners and can be solved without any further relations using the shock-capturing approach.

In order to treat the peripheral shock of the external problem as a sharp discontinuity, equation (4) is first normalized between the surface of each wedge and the shock. This requires a separate coordinate transformation for each of the two regions outlined by points 1-2-3-4-1 and 5-6-7-8-5 in figure 4. The necessary equations will be developed for the horizontal region only, since the derivation of the analogous equations for the vertical region is the same.

The required transformation is

$$\left. \begin{array}{l} \zeta = \zeta \\[2mm] \lambda = (\eta - \eta_b)/[\eta_s(\zeta,\xi) - \eta_b] \\[2mm] \xi = \xi \end{array} \right\} \tag{5}$$

and when applied to equation (4) yields

$$E_\zeta + F_\lambda + G_\xi + H = 0 \tag{6}$$

where

$$E = E^*$$

$$F = E^*\lambda_\zeta + F^*\lambda_\eta + G^*\lambda_\xi$$

$$G = G^*$$

$$H = H^* - E^*\lambda_{\zeta_\lambda} - G^*\lambda_{\xi_\lambda}$$

$$\lambda_\zeta = -\lambda(\eta_s)_\zeta/(\eta_s - \eta_b)$$

$$\lambda_\eta = 1/(\eta_s - \eta_b)$$

$$\lambda_\xi = -\lambda(\eta_s)_\xi/(\eta_s - \eta_b)$$

$$\lambda_{\zeta_\lambda} = -(\eta_s)_\zeta/(\eta_s - \eta_b)$$

$$\lambda_{\xi_\lambda} = -(\eta_s)_\xi/(\eta_s - \eta_b)$$

The equation of the shock is $\dot{y}_s = y_s(x,z)$, and the quantity $(\eta_s)_\zeta$ of equation (6) can be expressed as a function of the derivatives $(y_s)_x$ and $(y_s)_z$ as follows:

$$(\eta_s)_\zeta = \frac{y_\zeta - (y_s)_x - (y_s)_z z_\zeta}{z_\eta (y_s)_z - y_\eta} \tag{7}$$

where

$$(y_s)_z = \frac{y_\xi + y_\eta (\eta_s)_\xi}{z_\xi + z_\eta (\eta_s)_\xi}$$

$$y_\zeta = \frac{y}{\zeta}$$

$$y_\eta = \frac{y}{\eta e}$$

$$y_\xi = - \frac{\eta \tan \Lambda_1}{\xi e}$$

$$z_\zeta = \frac{z}{\zeta}$$

$$z_\eta = \frac{\xi \tan \Lambda_2}{\eta e}$$

$$z_\xi = \frac{z}{\xi e}$$

$$y = \frac{\eta \zeta (1 - \xi \tan \Lambda_1)}{e}$$

$$z = \frac{\xi \zeta (1 + \eta \tan \Lambda_2)}{e}$$

The quantity $(\eta_s)_\xi$ is evaluated numerically and $(y_s)_x$ is computed from the Rankine-Hugoniot equations:

$$\left(y_s\right)_x = \left[u_\infty\left(v_\infty - w_\infty\left(y_s\right)_z\right) \right.$$

$$\left. + \tilde{u}_1\sqrt{\left(v_\infty - w_\infty\left(y_s\right)_z\right)^2 + \left(u_\infty^2 - \tilde{u}_1^2\right)\left(1 + \left(y_s\right)_z^2\right)} \right]\Big/\left(u^2 - \tilde{u}_1^2\right)$$

$$\tilde{u}_1^2 = \frac{\gamma^2 - 1}{4\gamma}\ \frac{p_1}{\rho_1}\left[\frac{p_2}{p_1} + \frac{\gamma - 1}{\gamma + 1}\right]$$

$$\rho_2 = \rho_1 \frac{\dfrac{p_2}{p_1} + \dfrac{\gamma - 1}{\gamma + 1}}{1 + \dfrac{\gamma - 1}{\gamma + 1}\dfrac{p_2}{p_1}}$$

$$\vec{q}_2 = \left(u_\infty - \left(y_s\right)_x a\right)\hat{\imath} + \left(v_\infty + a\right)\hat{\jmath} + \left(w_\infty - \left(y_s\right)_z a\right)\hat{k}$$

$$\left. \begin{array}{c} \\ \\ \\ \\ \\ \\ \end{array} \right\} \tag{8}$$

where

$$a = \frac{\left|\tilde{u}_1\right|\left(1 - \rho_1/\rho_2\right)}{\sqrt{\left(y_s\right)_x^2 + 1 + \left(y_s\right)_z^2}}$$

and the subscript ∞ indicates the free-stream condition.

Following the approach developed by Thomas et al. (ref. 3), it is only necessary to know the pressure behind the shock in order to propagate it. The remaining flow quantities can be found from equation (8). Shock pressure is determined by a finite-difference approximation of the governing partial differential equations at the shock (refs. 4 and 5).

Equation (4), which governs both corner flows (via shock-capturing), and equation (6), which governs only the external corner flow (via shock-fitting), are hyperbolic with respect to the conical coordinate ζ. These equations can therefore be solved iteratively until E_ζ^* of equation (4) and E_ζ of equation (6) are zero, indicating the establishment of conical flow.

The boundary condition at the surface of each wedge requires that the flow be tangent to it. Since an iterative procedure is employed to solve the governing equations, a simple Euler predictor/modified Euler corrector with one-sided normal derivatives is used at each surface. The following condition on the velocity components is imposed after the corrector step to satisfy tangency:

$$v = u \tan \delta_1 - w \tan \delta_1 \tan \Lambda_1; \text{ horizontal wedge}$$
$$w = u \tan \delta_2 + v \tan \delta_2 \tan \Lambda_2; \text{ vertical wedge}$$

The axial corner is treated as a multiple-valued point to account for the vortical singularity that exists there. Although pressure is continuous, density and velocity are discontinuous.

The computational boundaries for both the internal and external corner flows are shown in figure 4. Region I corresponds to the uniform free stream, region II to the horizontal wedge flow, region III to the vertical wedge flow, and region IV represents the unknown conical flow. Regions I, II, and III are known flow regions and are hyperbolic zones in the cross-flow planes. Region IV is unknown and elliptic in the cross-flow plane. It is the determination of this region that is the crux of the present problem.

RESULTS

Numerical results for the internal corner flow problem are shown in figures 5-10. These results were computed by Kutler (ref. 6) and Shankar and Anderson (ref. 7).

Some of the most recently published experimental data obtained for the corner-flow problem are by West and Korkegi (ref. 8). They tested an equal wedge angle $(\delta_1 = \delta_2 = 9.49°)$ configuration in Mach 2.98 flow over a Reynolds number range from 0.4×10^6 to 60×10^6, which included laminar, transitional, and turbulent boundary layers. A numerical solution for this same case was obtained, and the shock wave and slip surface structure are compared with the high Reynolds number experiment in figure 5.

The inviscid embedded shock is slightly concave when viewed from the origin falling inside the location of the corresponding experimental shock. The corner shock, which is slightly convexed when viewed from the origin, also falls inside the experimental shock. The positions of the experimental and numerical wedge shocks agree exactly. It appears, therefore, that the displacement effects of the boundary layer in the region bounded by the corner and embedded shocks result in an effective thickening of the body, and this forces the shock structure outward.

The location of the slip surfaces for this case can be found from plots of density and is shown as the thin double line in figure 5 stretching from the triple point to the origin. The slip surface is slightly curved and asymptotically approaches the bisector near the origin. The experimental shear layer is also curved but appears to merge before the origin is reached. Since the positions of the numerical and experimental triple points are different, the comparison between the inviscid slip surface and viscous shear layer, which originate at the triple points, is unfair. But, qualitatively, their basic shapes are the same.

A comparison of the numerical and experimental (turbulent boundary layer) surface pressures is shown in figure 6. The first pressure rise in

the experimental data (decreasing) indicates the onset of separation. This is followed by a reduced gradient region that indicates separation and again a rapid pressure rise that indicates reattachment. The pressure between the reattachment point and the origin is greater than that of the inviscid result. This higher pressure indicates an apparent thickening of the body in this region due to boundary-layer displacement effects.

Nangia (ref. 9) performed an experimental study on the wave interactions in supersonic intakes and obtained some rather interesting data. Figures 7-9 are numerical solutions which compare with Nangia's results. Figure 7 is a pressure contour plot for an unswept configuration with $\delta_1 = -5°$ and $\delta_2 = 7.5°$ for a Mach number of 3. It is interesting to note that the wave structure does not exhibit any corner shock or slip surfaces. This appears to be correct because changes through the expansion fan occur isentropically. However, an auxiliary compression wave is formed in the corner region. The wedge expansion fan, after the interaction with the wedge shock, turns away from the axial corner and is concave when viewed from the origin, whereas the wedge shock turns toward the axial corner and appears to be slightly convex.

The inviscid numerical wave structure compares very well with the experimental results of Nangia. The auxiliary compression fan in the corner region, as predicted by the numerical solution, is not observed in the experimental results, however.

A pressure contour plot for a $\Lambda = 30°$, $\delta_1 = 5°$, and $\delta_2 = 7.5°$ configuration at a Mach number of 3 is shown in figure 8. The numerical solution is again compared with the experimental data of Nangia. The computed surface-pressure distribution for both the horizontal and vertical wedges is compared with Nangia's experimental measurements in figure 9.

The final case considered on the internal corner problem consists of a $\Lambda = 30°$, $\delta_1 = -5°$, and $\delta_2 = 7.5°$ configuration at a Mach number of 3. The pressure contour plot of the numerical solution is shown in figure 10. The wedge expansion fan, after interacting with the wedge shock, turns away from the axial corner and appears to be concave when viewed from the origin. The intersecting wedge shock is deflected towards the axial corner under the influence of the wedge expansion fan. An auxiliary weak shock is formed in the corner region which merges with the weak embedded shock and forms a strong shock near the horizontal wedge surface. The shock impingement on this surface is nearer the axial corner than the wedge shock. The strength of the impinging shock appears to increase with increasing sweep angle. Furthermore, the interference region decreases as the sweep angle increases.

Numerical solutions for two external corner configurations were generated and are shown in figures 11-14. Results are presented for both the shock-capturing and shock-fitting techniques. Figure 11 shows the shock shape and cross-flow sonic line for an unswept equal-angled ($\delta_1 = \delta_2 = 10°$) configuration at a Mach number of 3. The surface-pressure distribution for this case compared to linear theory is shown in figure 12.

The shock and cross-flow sonic-line locations for a swept ($\Lambda_1 = \Lambda_2 = 30°$), equal wedge angle ($\delta_1 = \delta_2 = 10°$) configuration at Mach number 3 is

shown in figure 13. The shock-capturing results are almost identical to the shock-fitting solution. The surface pressure distribution for this configuration is shown figure 14, and again both the shock-capturing and shock-fitting results agree.

All of the numerical results presented here were obtained on serial machines but employed a numerical procedure which is particularly well suited for the parallel processing philosophy. Should the computing power of an ILLIAC IV be required for a more complicated problem, such as a multiple-corner configuration, some of the coding techniques used for the solutions presented here could easily be applied.

REFERENCES

1. MacCormack, R. W.: The Effect of Viscosity in Hypervelocity Impact Cratering. AIAA Paper 69-354, 1969.

2. Kutler, P., and Lomax, H.: Shock-Capturing, Finite Difference Approach to Supersonic Flows. J. of Spacecraft and Rockets, vol. 8, 1971, pp. 1175-1182.

3. Thomas, P. D., Vinokur, M., Bastianon, R., and Conti, R. J.: Numerical Solution for the Three-Dimensional Inviscid Supersonic Flow of a Blunt Delta Body. AIAA Jour., vol. 10, no. 7, July 1972, pp. 887-894.

4. Kutler, P., Reinhardt, W. A., and Warming, R. F.: Multishocked, Three-Dimensional Supersonic Flowfields with Real Gas Effects. AIAA Jour., vol. 11, no. 5, May 1973, pp. 657-664.

5. Kutler, P.: Computation of Three-Dimensional, Inviscid Supersonic Flows. Computational Methods in Fluid Dynamics, Lecture Notes in Physics, AGARD, 1975. (To be published.)

6. Kutler, P.: Supersonic Flow in the Corner Formed by Two Intersecting Wedges. AIAA Jour., vol. 12, 1974, pp. 577-578.

7. Shankar, V., and Anderson, D. A.: Numerical Solutions for Inviscid Supersonic Corner Flows. Final Report ISU-ERI-AMES-74090, May 1974.

8. West, J. E., and Korkegi, R. H.: Supersonic Interactions in the Corner of Intersecting Wedges at High Reynolds Numbers. AIAA Journal, vol. 10, May 1972, pp. 652-656.

9. Nangia, R. K.: Three-Dimensional Wave Interactions in Supersonic Intakes. Second International Symposium on Air Breathing Engines (Sheffield, United Kingdom), March 1974.
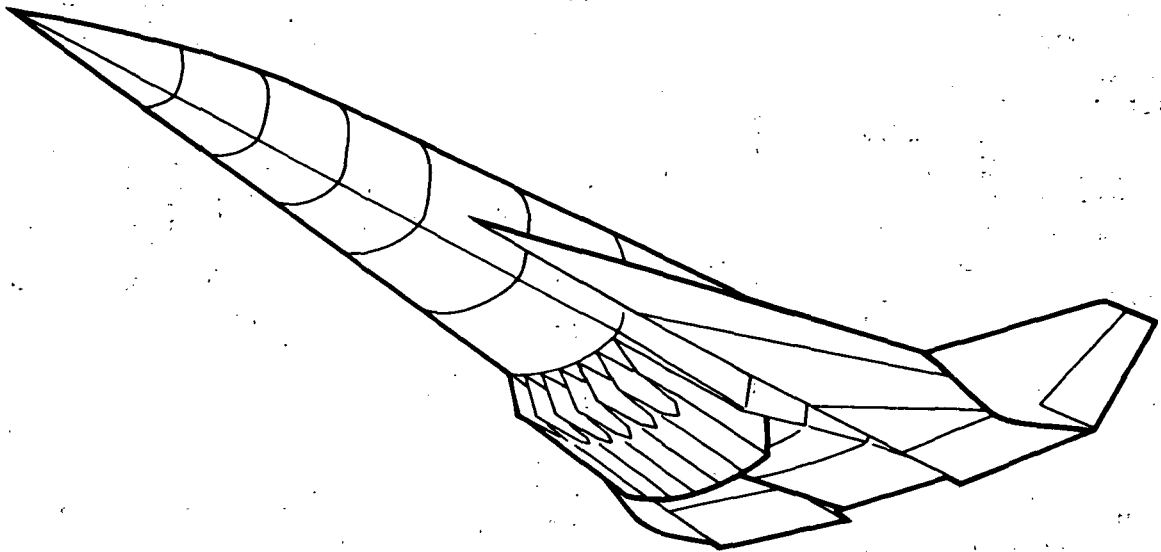
Fig. 1 Hypersonic airbreathing aircraft

$$\delta_1 \begin{cases} >0: \text{COMPRESSION SURFACE} \\ <0: \text{EXPANSION SURFACE} \end{cases}$$
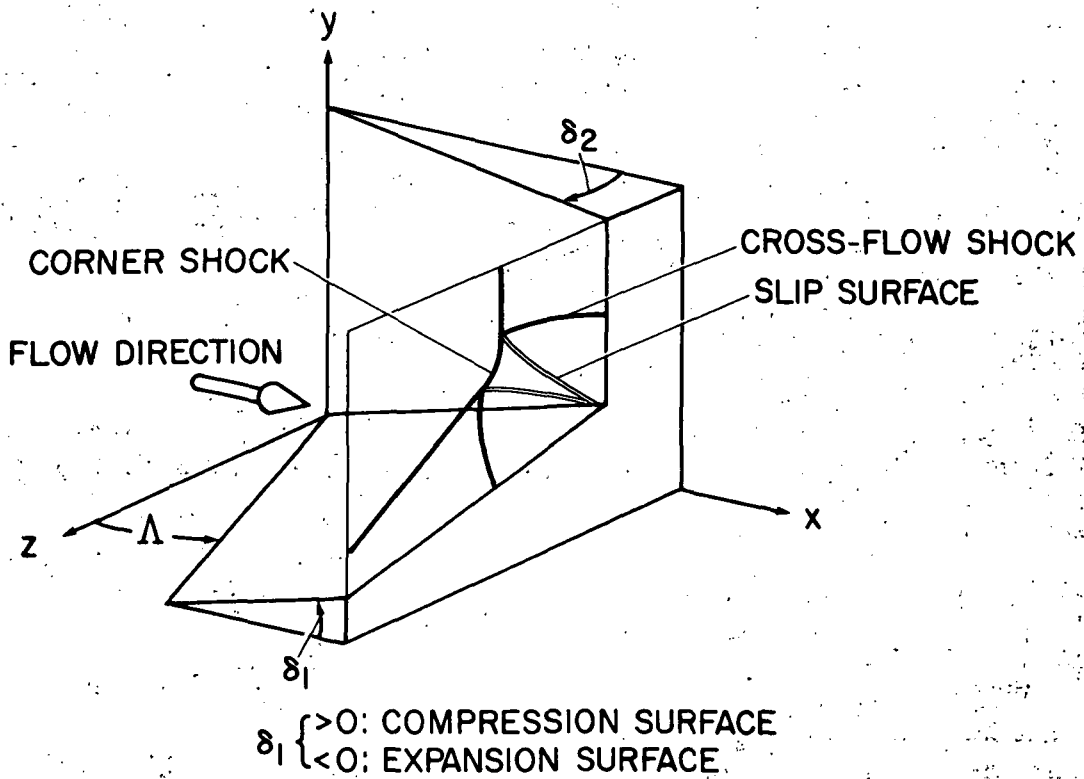
Fig. 2 Coordinate system and wave structure for internal axial corner.
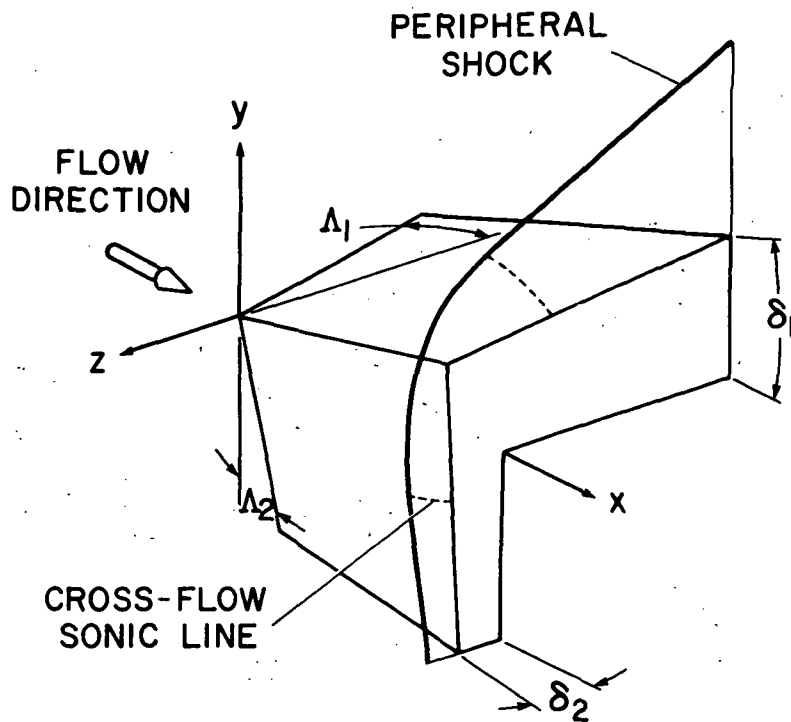
Fig. 3 Coordinate system and shock structure for external axial corner.

I   FREE STREAM
II ⎫ SLIDING
III ⎭ WEDGE FLOW
IV UNKNOWN

INTERNAL AXIAL CORNER

EXTERNAL AXIAL CORNER
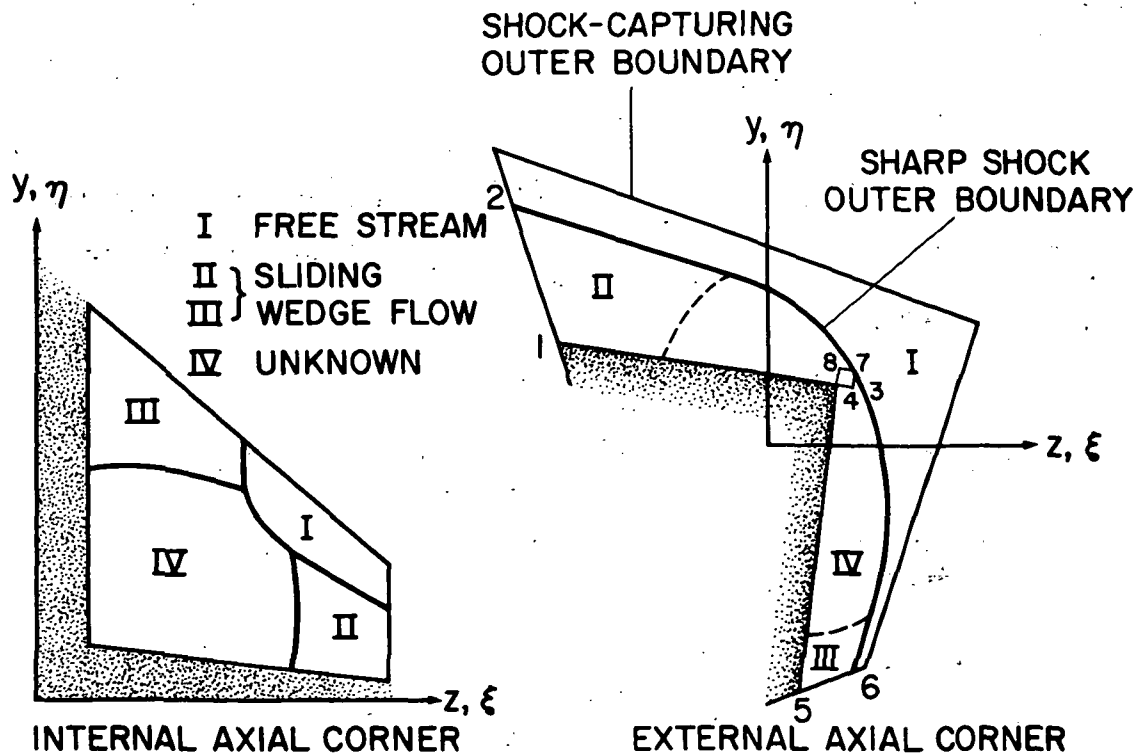
Fig. 4 Computational boundaries for internal and external axial corners.
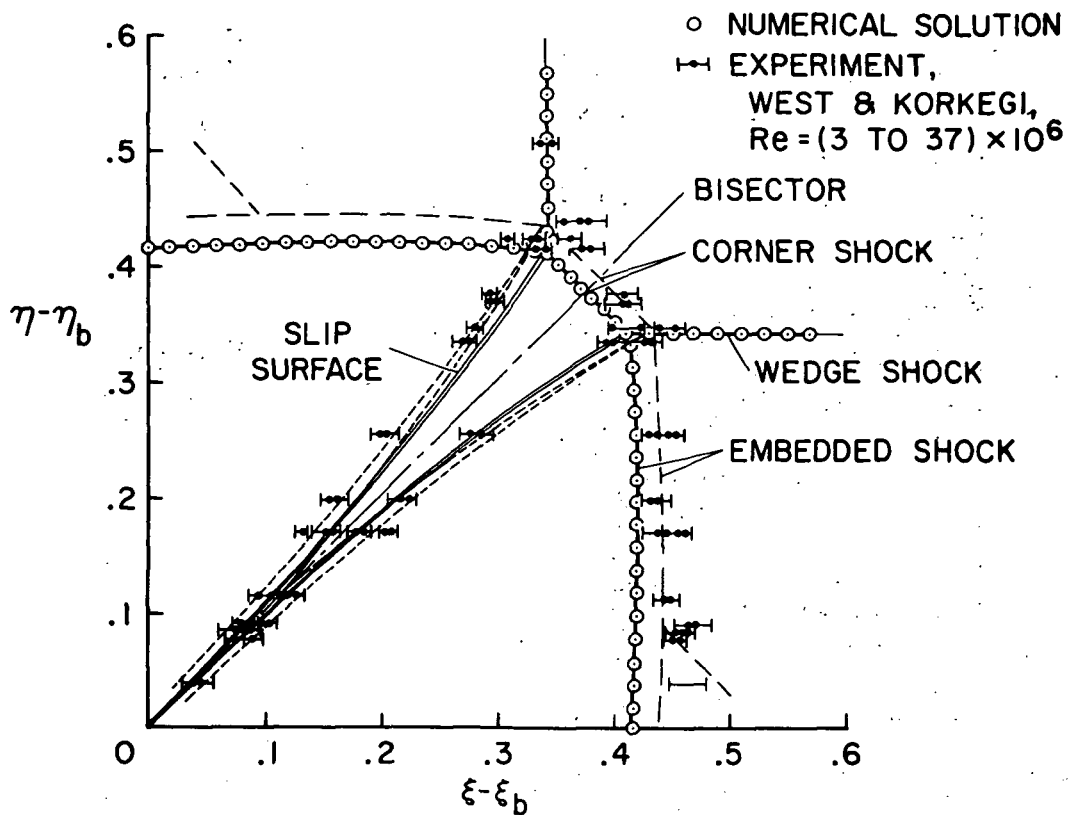
Fig. 5 Comparison of numerical and experimental shock patterns; $M = 2.98$, $\delta_1 = \delta_2 = 9.49°$.
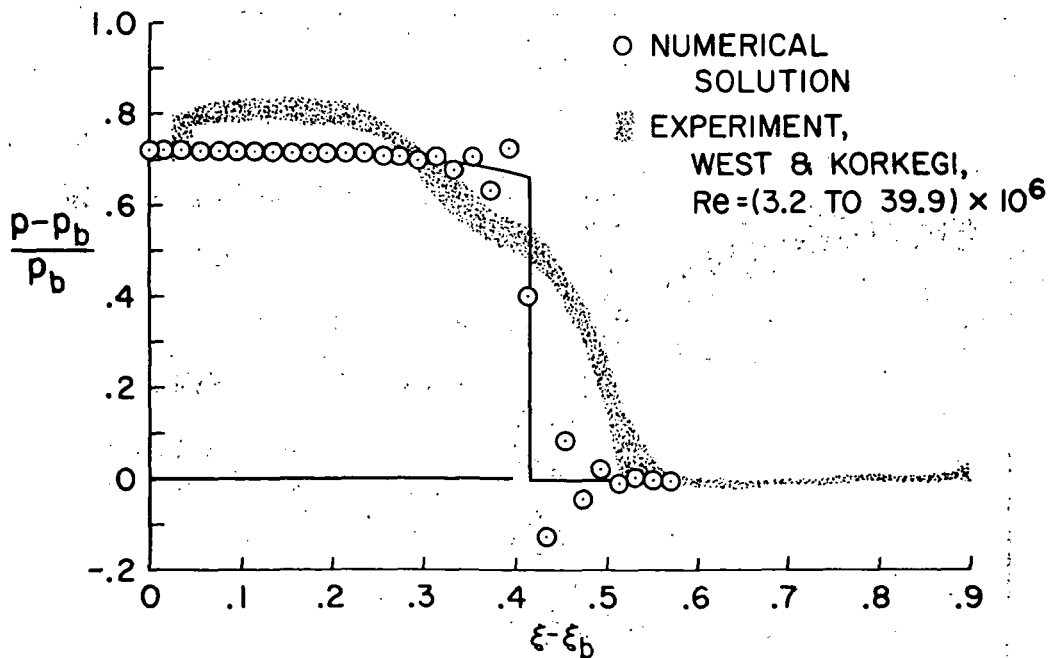
Fig. 6 Comparison of numerical and experimental surface-pressure distribution; $M = 2.98$, $\delta_1 = \delta_2 = 9.49$, $\Lambda = 0°$.
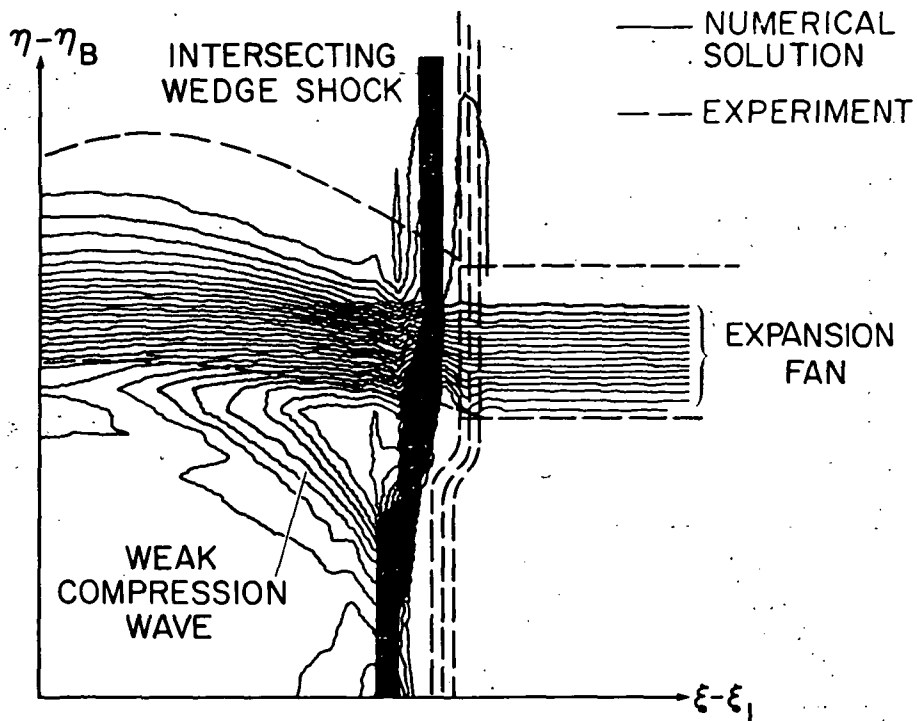
Fig. 7 Comparison of numerical and experimental wave structure; M = 3, $\delta_1 = -5°$, $\delta_2 = 7.5°$, $\Lambda = 0°$.
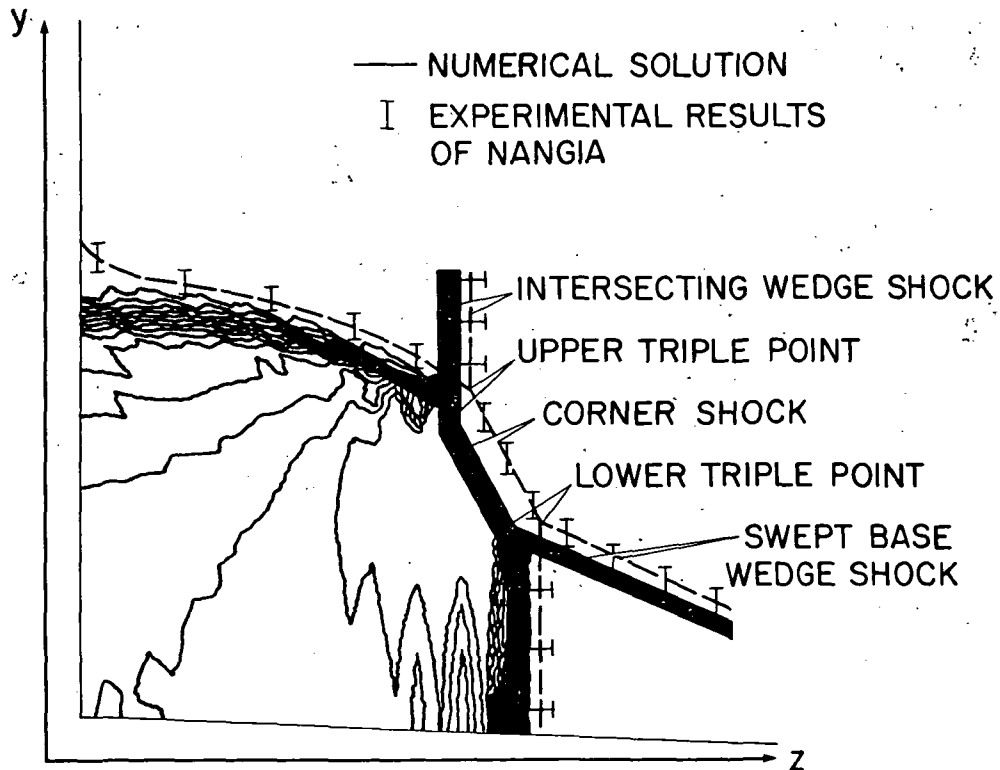
Fig. 8 Comparison of numerical and experimental shock structure; M = 3, $\delta_1 = 5°$, $\delta_2 = 7.5°$, $\Lambda = 30°$.
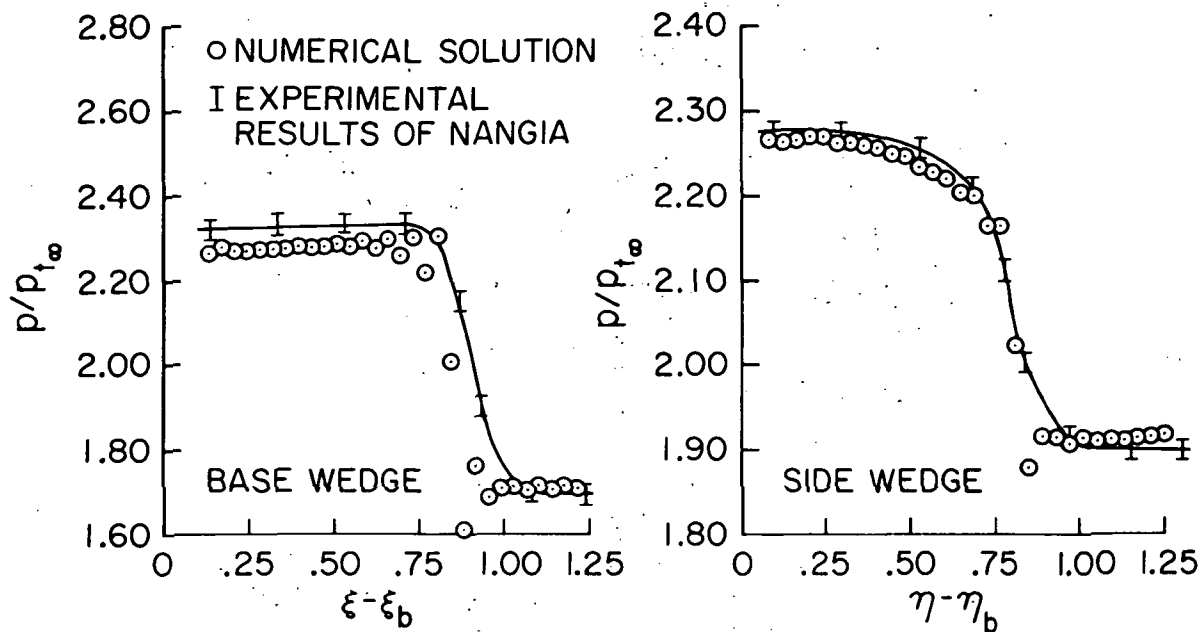
Fig. 9 Comparison of numerical and experimental surface-pressure distribution; $M = 3$, $\delta_1 = 5°$, $\delta_2 = 7.5°$, $\Lambda = 30°$.
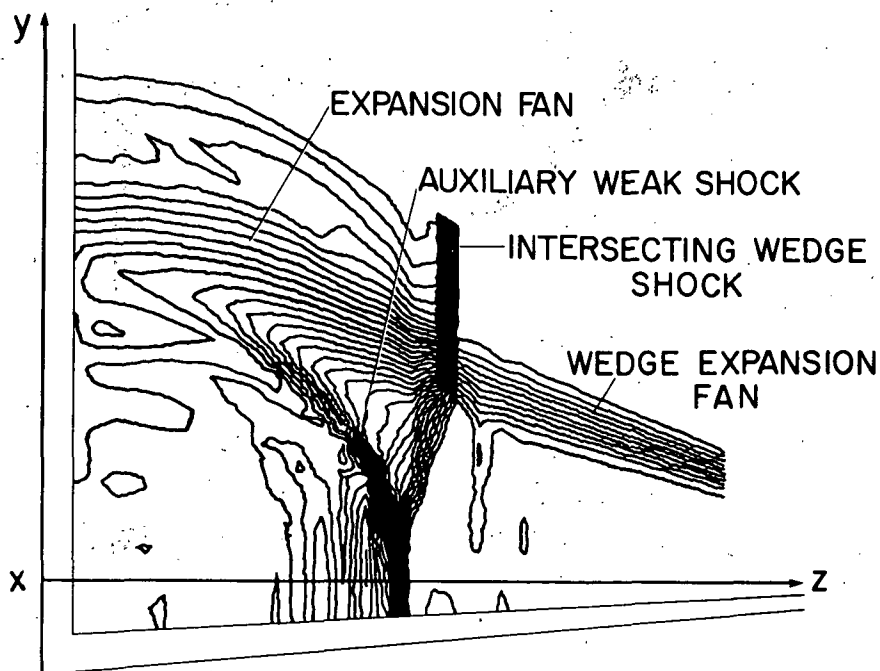
Fig. 10 Pressure contour plot of computational plane; $M = 3$, $\delta_1 = -5°$, $\delta_2 = 7.5°$, $\Lambda = 30°$.
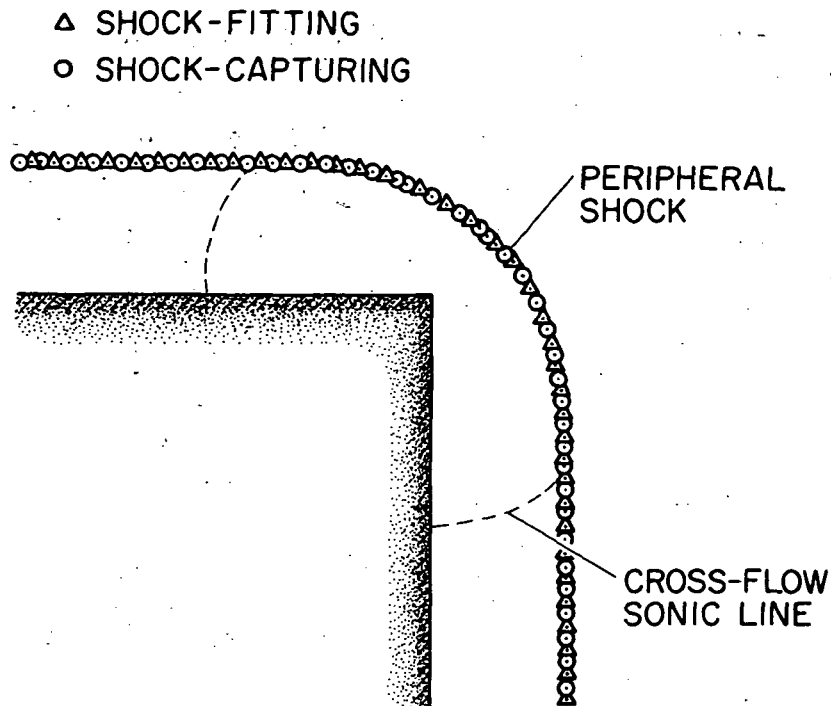
Fig. 11 Shock structure for symmetric external corner; $M = 3$, $\delta_1 = \delta_2 = 10°$, $\Lambda_1 = \Lambda_2 = 0°$.
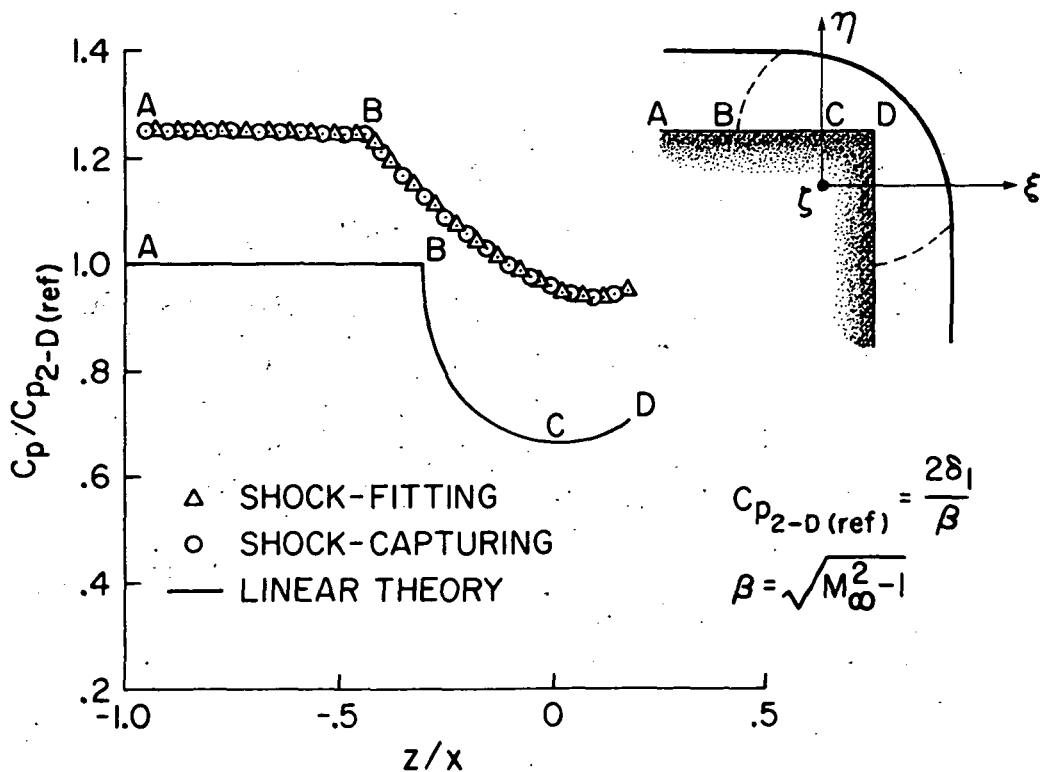

Fig. 12 Surface-pressure distribution for symmetric external corner; $M = 3$, $\delta_1 = \delta_2 = 10°$, $\Lambda_1 = \Lambda_2 = 0°$.
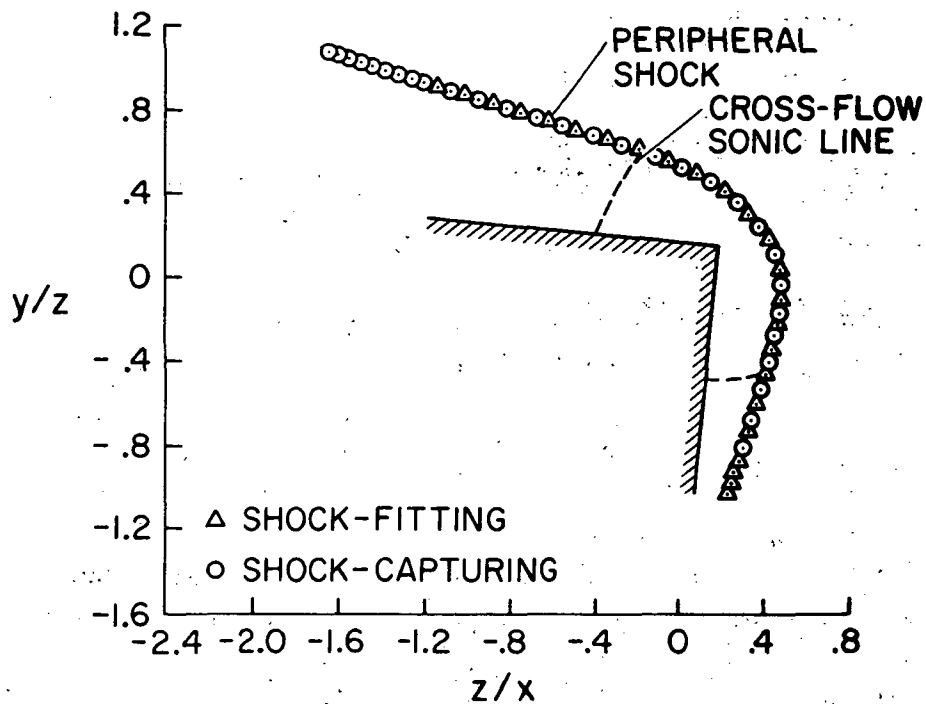
Fig. 13 Shock structure for swept external corner; $M = 3$, $\delta_1 = \delta_2 = 10°$, $\Lambda_1 = \Lambda_2 = 30°$.
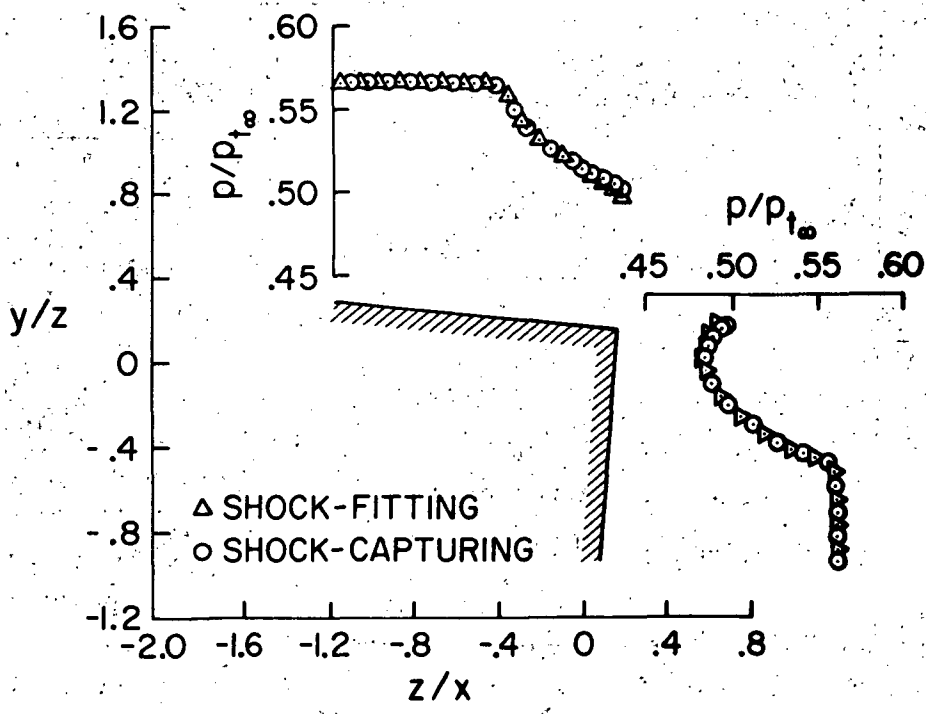
Fig. 14 Surface-pressure distribution for swept external corner; $M = 3$, $\delta_1 = \delta_2 = 10°$, $\Lambda_1 = \Lambda_2 = 30°$.